J Mater Sci (2019) 54:3558–3571

Metals

Microstructure and mechanical properties of a new cast nickel-based superalloy K4750 joint produced by gas tungsten arc welding process

Jilin Xie[1,2], Yingche Ma[1,*], Weiwei Xing[1], Meiqiong Ou[1], Long Zhang[1], and Kui Liu[1,*]

[1] Institute of Metal Research, Chinese Academy of Sciences, No. 72 Wenhua Road, Shenyang, China
[2] School of Materials Science and Engineering, University of Science and Technology of China, No. 96 Jinzhai Road, Hefei, China

Received: 28 June 2018
Accepted: 29 October 2018
Published online: 19 November 2018

ABSTRACT

The microstructures and mechanical properties of gas tungsten arc-welded joints of superalloy K4750 that has been newly developed were examined. The microsegregation pattern during solidification of the fusion zone indicated that Fe was prone to segregate into the dendritic core, while Nb, Mo, Ti, W and Si were rejected into the dendritic boundary. The phase transformation sequence of the K4750 alloy fusion zone was L → L + γ → L + γ +(Ti,Nb)C → γ + (Ti,Nb)C. Heat-affected zone (HAZ) examination shows it consisted of partially melted zone with liquated MC carbides and liquated grain boundaries. Cracking-free HAZ microstructure suggested that K4750 alloy possess excellent HAZ cracking resistance properties. Relatively low concentration of Al and Ti results in the excellent cracking resistance properties of the alloy. Vickers microhardness of as-welded joint is lower than that of post-weld heat treatment (PWHT) joint across the whole joint due to the absence of 50 nm spherical γ′ particles formed during PWHT. Tensile properties of as-welded joints are comparable to PWHT joints in terms of the ultimate tensile strength and elongation.

Introduction

Ni-based superalloys are intensively used in aero-engine hot components such as turbine disk, casings and blades [1, 2]. Inconel 718 superalloy is one of the most widely used Ni-based superalloy precipitation strengthened by γ″ and γ′ phases. The bearing temperature limitation of Inconel 718 is 650 °C because the γ″ is thermally instable when temperature is above 650 °C, and this phase will transform to stable δ phase which is harmful to high-temperature mechanical properties of the alloy [3–5].

Recently, in order to meet the higher temperature requirements, the development of superalloys for higher working temperatures gained great attractions. Allvac® 718Plus™ is a γ′ hardened superalloy developed by ATI Allvac which offers a 55 °C improvement of temperature limitation compared to Inconel 718 alloy [6]. This alloy maintains many desirable features of alloy 718, including good

Address correspondence to E-mail: ycma@imr.ac.cn; kliu@imr.ac.cn

https://doi.org/10.1007/s10853-018-3081-y

workability, weldability and moderate cost. Nevertheless, superalloys for application at 750 °C are still under investigation [7].

A new cast Ni-based superalloy named as K4750 has been developed in China for aeroengine applications at temperature till 750 °C [8]. The alloy offers about 100 °C service temperature advantage over Inconel 718 and about 50 °C over Allvac® 718Plus™. This is because the novel designed alloy is a γ′ hardening cast Ni-based superalloy with the content of Ti + Al approximately 4.4 wt%. Titanium and Al are the main γ′ phase forming elements which are used to obtain high-temperature mechanical properties in superalloys [1].

Superalloys were generally considered difficult to be welded especially the precipitation-strengthened superalloy due to the heat-affected zone (HAZ) cracking during welding and subsequently post-weld heat treatment (PWHT) [9]. However, the welding is unavoidable during component fabrication and repairment, a weldable precipitation-strengthened superalloy, like IN 718 alloy, but without the temperature restriction is very attractive. The compositional and microstructural changes usually have significant effects on the welding characteristics of the alloy [10]. Hence, the objective of the present work was to systemically evaluate and understand the weldability of the novel designed superalloy, K4750, using gas tungsten arc welding process (GTAW). Since GTAW processing is one of the most widely used welding methods due to the economical friendly and operation flexibility [11].

Materials and methods

Materials and welding process

The plates and the filler metals used in the present work have the same chemical compositions and are shown in Table 1. The as-received plates of K4750 superalloy with the size of 250 × 136 × 4.5 mm were fabricated by vacuum induction melting (VIM). As-cast plates were machined into the size of 100 × 65 × 2.5 mm and solutionized at 1120 °C for 4 h followed by air cooling. Steel brushing was used to remove all oxidation products at the plate surfaces, and then, a groove was machined at the edge of the plate as shown in Fig. 1. Butt welding of the alloy was conducted by manual welding using direct current electrode positive GTAW processing. To avoid oxidation, shielding gas (Argon) with a purity of 99.99% was utilized at both sides of the plates. An Ø2.0 mm cerium-containing tungsten electrode and an Ø1.2 mm K4750 filler metal were used. The other detailed welding parameters are listed in Table 2. The post-weld heat treatment procedures of the as-welded joints are as follows:1120 °C/4 h air cooling + 800 °C/20 h air cooling.

Thermodynamic calculation and DTA analysis

The 2016b version thermal-calc software with 8.3 version TTNi8 Ni-based alloy database was used to calculate the solidus, liquidus and the main phase precipitation temperature in the K4750 fusion zone. The simulation was performed under equilibrium condition with 10 °C per step from 600 to 1400 °C. At each temperature step, the program determines the equilibrium phase according to the lowest Gibb's energy. For comparison, the differential thermal analysis (DTA) was also employed to estimate the transformation temperature of main phase in the as-welded joint fusion zone. The heating and cooling rates of the DTA test were set as 10 °C/min.

Microstructure evaluation and mechanical properties test

Metallography samples of the joints were cut and polished for microstructural study. Thereafter, the specimens were chemical etched by a solution of 20 g $CuSO_4$ + 150 ml HCl + 80 ml H_2O. The joint

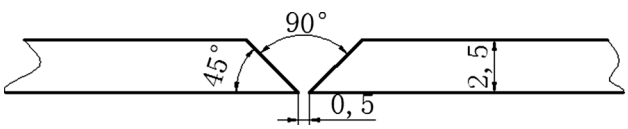

Figure 1 Schematic of the butt welding joints.

Table 1 Chemical compositions of the as-welded plates and the filler metals(wt%)

Elements	C	Cr	W	Mo	Al	Ti	Nb	Fe	B	Ni
Content	0.1	19.9	3.2	1.3	1.4	3.0	1.5	4.3	0.0075	Bal.

Table 2 GTAW processing parameters

Welding current (A)	Welding voltage (V)	Nozzle diameter (mm)	Argon flow rate(L/min)
45	10–12	Ø8–16	8–10

microstructures were examined and analyzed by optical microscope (OM), scanning electron microscope (SEM) and JEM-2100 transmission electron microscope (TEM) with energy-dispersive spectrometer (EDS). Electron-probe microanalyzer (EPMA/WDS) with wave spectrometer was used to illustrate the element distributions at dendritic cores and dendritic boundaries. The TEM samples were produced by twin-jet polishing with 10% perchloric acid in 90% methyl alcohol at the temperature of − 18 °C and the voltage of 15 V.

Vickers microhardness test was conducted at the middle line of the metallography samples in the transverse direction with the load of 500gf and the dwell time of 15 s by a microhardness tester. The distance between two indentations is 0.5 mm in the fusion zone and base metal, 0.25 mm in the HAZ. The room-temperature tensile strength of the joint was measured using Instron 5582 machine.

Results and discussion

Thermodynamic calculation and DTA results of K4750 superalloy

Thermodynamic calculations were performed to predict the transformation temperatures of various phases formed in K4750 alloy, and the calculated equilibrium phase diagram is presented in Fig. 2. The solidus and liquidus temperatures are 1269 °C and 1350 °C, respectively. There are about 30 wt% γ′ phases precipitated at 1003 °C in the alloy. The MC phase started to precipitate at the end of the solidification process, and the $M_{23}C_6$ carbide was formed at 960 °C. The η phase, which was usually considered detrimental to mechanical properties, was calculated precipitated at 850 °C. The α-Cr phase and P phase were also predicted to appear at 680 °C and 628 °C, respectively.

At the same time, the DTA experiment was employed to physically simulate the precipitates transformation temperatures of K4750 alloy. The DTA results are shown in Fig. 3. As can be seen from Fig. 3a, the solidus temperature is 1306 °C which is obtained from the intersection of the extrapolated base line and the tangent of the maximum curve slop in the heating curve. The liquidus temperature is 1348 °C obtained from the first sharp inflection point of the cooling curve as seen in Fig. 3b. The 1032 °C marked in the heating curve is considered as the γ′ phase dissolution temperature. The carbides dissolution temperature is 1331 °C. And the temperature of 1355 °C is considered as the gamma matrix completely dissolved temperature. Moreover, from the cooling curve, three major phase transformation temperatures were observed. The sharp peak temperature 1339 °C is related to the abundant formation of gamma matrix. The carbides and the γ′ phase precipitation temperatures are considered at 1294 °C and 969 °C, respectively.

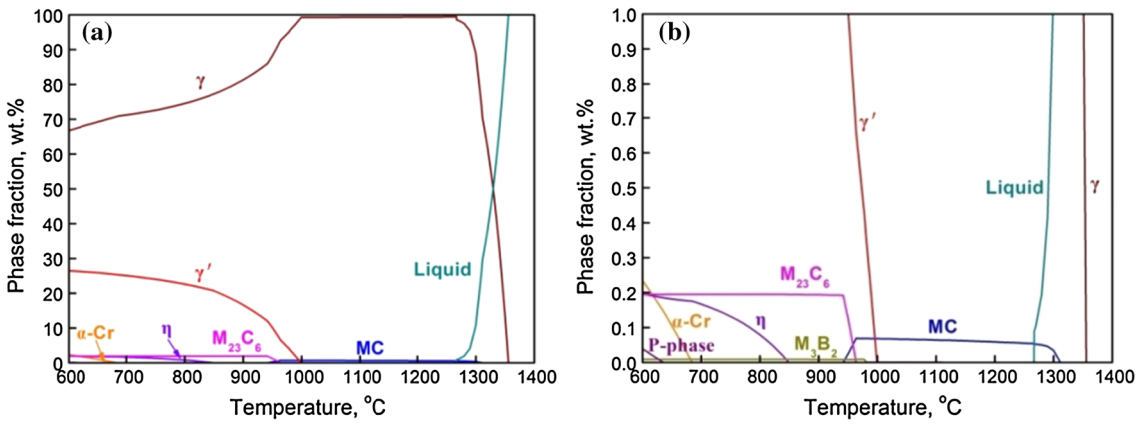

Figure 2 Thermodynamic phase diagram of the K4750 alloy. **a** Overall diagram, **b** partial diagram.

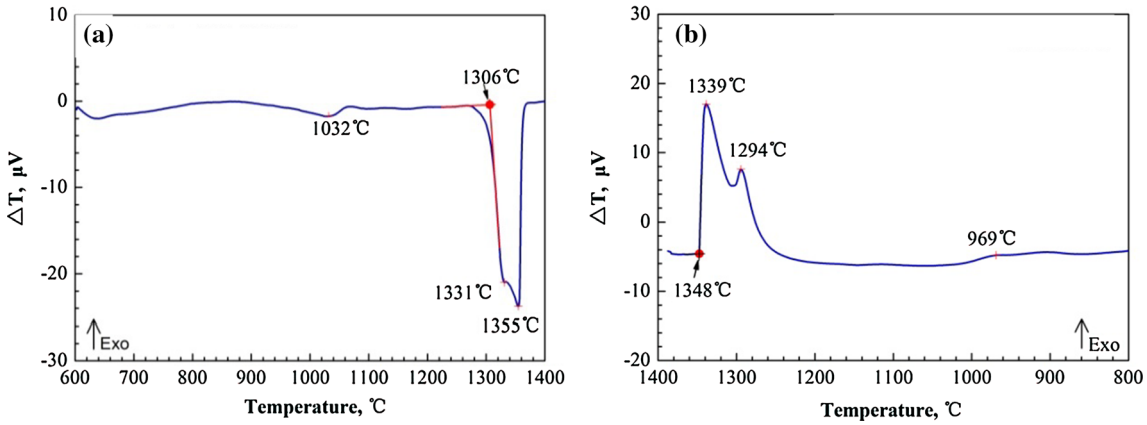

Figure 3 DTA results of the K4750 alloy. **a** On-heating and **b** on-cooling processes.

Table 3 Main phase precipitation temperatures in K4750 alloy

Phase	Precipitation temperature (°C)	
	Modeling	DTA
Liquidus	1350	1348
Solidus	1269	1306
MC	1315	1294
γ'	1003	969
M_3B_2	995	–
$M_{23}C_6$	960	–
η	850	–
α-Cr	680	–
P phase	628	–

The phase transformation temperatures of K4750 alloy determined through thermodynamic modeling and differential thermal analysis (DTA) are summarized in Table 3. There are some differences in the results between these two methods. For example, transformation temperature peaks of some phases such as M_3B_2 borides, η phase, α-Cr and P phase were not identified in DTA curves. Two factors can be used to explain the difference. One is that the content of these precipitates is too small that the heat change during heating or cooling process of the DTA analysis is hard to be identified. This result was also mentioned in other published works that the DSC curve is very difficult to note the small thermal effects of tiny volume fraction carboborides [12]. The other is that thermal-calc results are based on the thermodynamic equilibrium solidification in each step. But the alloy test during heating or cooling in DTA analysis is in a non-equilibrium state. The phases predicted by thermocalculations may be suppressed during the non-equilibrium solidification. So it is unable to reveal the precipitation of these phases on the cooling curve of DTA analysis. Furthermore, it can be deduced that these phases will not form in the weld fusion zone since the solidification of the as-deposited filler metal during actual welding process is a non-equilibrium process. Yin et al. [13] also reported that because of the non-equilibrium rapid solidification of the weld metal, few amount of phases predicated by thermal-calc were formed. In addition, the main phase transformation temperatures obtained from the cooling curve are lower than those from the heating curve due to the superheating and supercooling effects on the phase transformation.

Microstructures of pre-weld heat-treated alloy

Figure 4 shows the microstructure of as-received base metal. As mentioned above, the as-received base metals were solutionized at 1120 °C for 4 h followed by air cooling. The precipitations with the shape of blocky and bar are randomly distributed inside the grains or at the grain boundaries. It is illustrated by EDS spectrum shown in Fig. 4c that these precipitations are Nb- and Ti-rich MC-type carbides. It can be seen from Table 3 that MC-type carbides precipitation temperature is higher than the solidus temperature; therefore, the MC-type carbides observed in the pre-weld heat-treated alloy are unable to dissolve by pre-weld solution heat treatment. The SEM image of the pre-weld heat-treated alloy did not reveal the presence of other constituents in the matrix of the alloy. The reason is that the pre-weld heat-treated

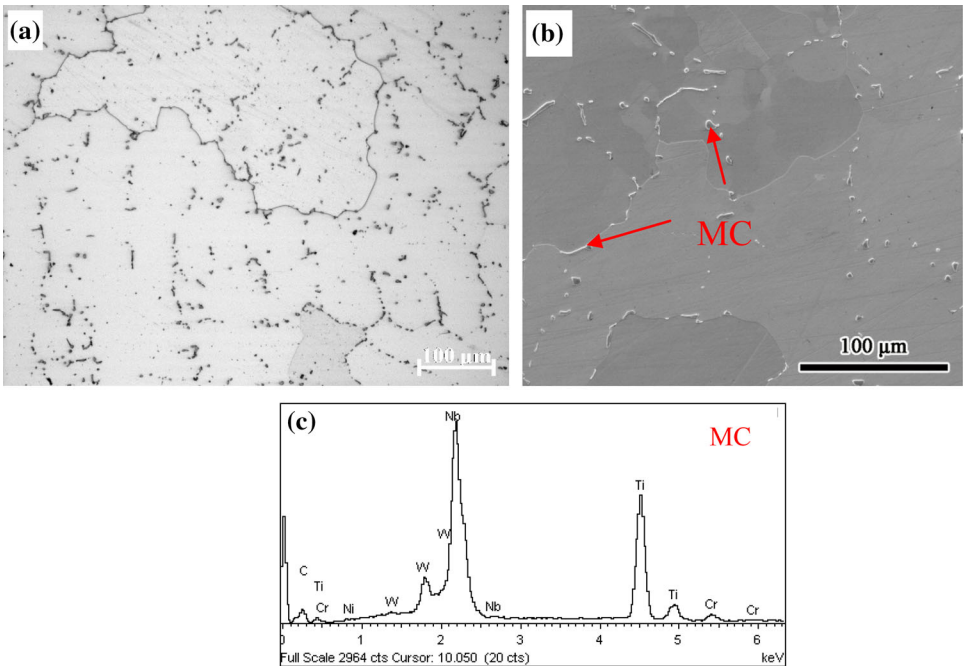

Figure 4 Microstructure of the base metal. **a** OM image of the base metal, **b** SEM images of the base metal **c** EDS spectrum of the MC-type carbides.

Figure 5 Macrostructure of the as-welded joint.

temperature in the present work is 1120 °C which is above the dissolution temperature of other precipitates.

Fusion zone solidification

Figure 5 shows typical macromorphology of the as-welded joint. No cracks were detected at the fusion zone (FZ) and the heat-affected zone (HAZ) of the joints. It demonstrated that the K4750 alloy has good resistance to solidification cracking and liquation cracking.

Figure 6 depicts the microstructure of as-welded joint fusion zone. Figure 6a shows that the γ matrix is formed in a dendritic mode. The columnar-to-equiaxed transition (CET) also can be clearly distinguished. The equiaxed dendrites are mainly at the interior fusion zone, while the columnar dendrites are mainly at the fusion boundary. In addition, the MC-type carbides, which are mainly distributed at the dendritic boundaries, are the major interdendritic constituents in the as-welded fusion zone as illustrated in Fig. 6b. It was difficult to identify the MC-type carbide by SEM/EDS analysis, due to their small size; therefore, TEM analysis was performed on the particles and is shown in Fig. 6c, d. The energy spectrum analysis shown in Fig. 6d demonstrated that the particles were significantly enriched in Nb, Ti and also with small amount of W and Mo. The electron diffraction patterns of these particles reveal that their crystal structure is FCC with the lattice constant $a = b = c = 0.4390$ nm, which is between that of TiC (0.4327 nm) and NbC (0.4470 nm), so these carbides might be (Ti, Nb)C. The results showed that the carbides in the fusion zone have same composition as those in the base metal but with smaller size due to the rapid solidification rate during weld cooling. There are no other precipitates observed in the fusion zone which is contrary to the prediction by the thermocalculations in Fig. 2. Here, the phase transformation sequence of K4750 alloy fusion zone is as follows: $L \rightarrow L + \gamma \rightarrow L + \gamma + (Ti,Nb)C \rightarrow \gamma + (Ti,Nb)C$. Another important factor affecting the final microstructure in fusion zone is the alloying element

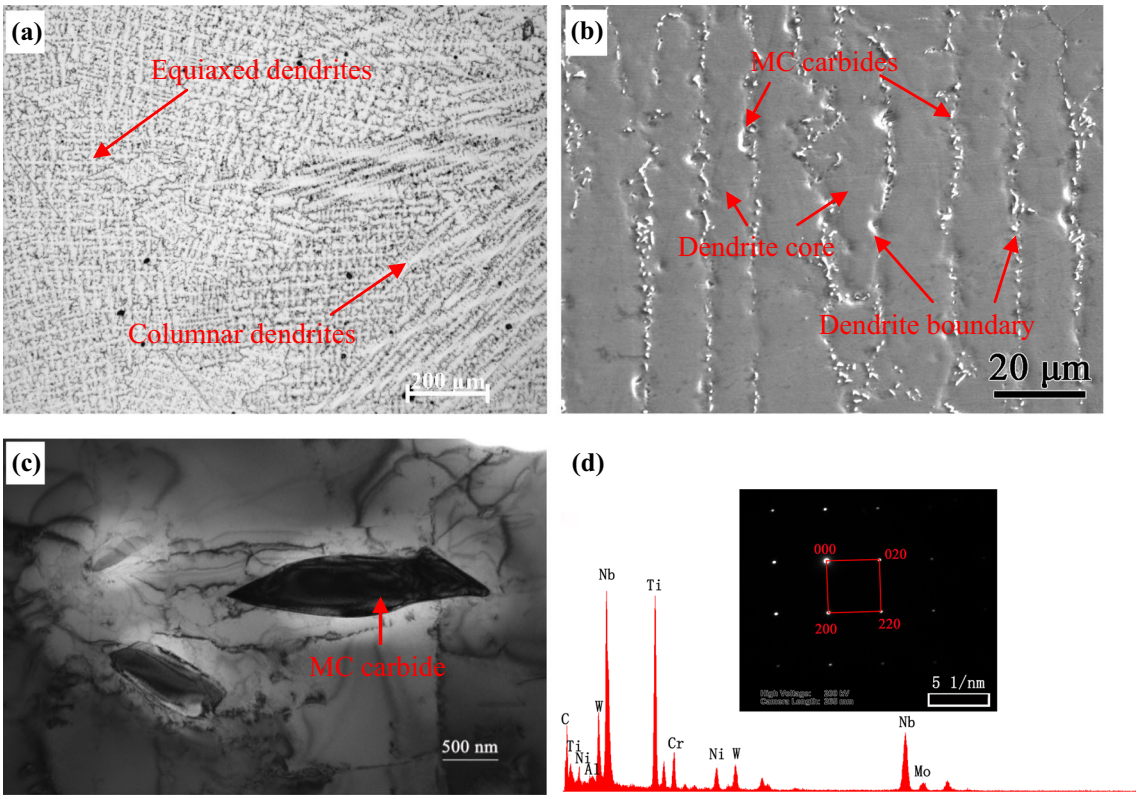

Figure 6 Microstructure of the as-welded joint fusion zone. **a** OM microstructure of FZ, **b** SEM microstructure of FZ, **c** TEM image of MC carbides, **d** EDS spectrum of the MC carbide marked in figure c and the inset is the SADP taken along the [001] axis.

segregation across the dendrite cores and dendrite boundaries. The partition coefficient k was used to describe segregation behavior of elements between liquid and solid during solidification. The alloying elements which have a value of $k < 1$ reveal the tendency to segregate in the interdendritic area, whereas the elements with value of $k > 1$ are prone to segregate to the dendritic core. Formally, it is calculated by the composition of the solid C_S divided by the composition of the liquid C_L in the equilibrium state [14]. As mentioned above, the solidification of the weld fusion zone is under a non-equilibrium condition. So the k values were calculated by using Scheil equation $k = C_S/C_o$. The solid composition C_S was got from the dendritic core composition C_{core}; thus, the partition coefficient k was from the ratio of C_{core} to C_o in weld fusion zone.

The chemical compositions of dendritic cores are listed in Table 4 as well as the values of partition coefficient k. As a comparison, the elements partition coefficients in superalloys IN 718 and IN 718P weld fusion zone are also listed in Table 4. As can be seen from Table 4, the elements Ni and Cr had the partition coefficient k very close to unity, indicating almost no segregation during solidification. And the elements Si and Nb had the k value less than unity, which implies that these elements segregated strongly into the interdendritic liquid during solidification. Molybdenum, Al, W and Ti also segregated into interdendritic liquid but to a smaller degree compared to Si and Nb. Iron has k value greater than unity indicating that it would segregate to dendrite core. The microsegregations of the alloying elements are in accordance with those in the IN 718 [15] and IN 718P fusion zones to some extent [16], where Si, Nb and Ti were found to segregate in the dendritic boundary and Fe segregated in the dendritic core. However, the segregation degree of these elements in electron beam-welded IN 718P fusion zone is smaller than those in the GTAW-welded K4750 and IN 718 fusion zone with k values closer to unity.

The observation of fine equiaxed dendrites in the weld center and of columnar dendrites at regions close to fusion boundary (Fig. 6a) is mostly related to thermal gradient (G) and cooling rate or growth rate (R). As we know, the degree of undercooling in a

Table 4 Chemical compositions (wt%) in the dendritic core and the partition coefficients k of K4750, IN 718 and IN 718P superalloys

Elements	Ni	Fe	Cr	Al	Si	W	Nb	Ti	Mo
Dendritic core	66.282	4.948	20.445	0.971	0.012	1.885	0.598	1.821	1.061
k	1.01	1.15	1.03	0.8	0.4	0.6	0.399	0.607	0.742
k in IN 718 alloy [15]	1.00	1.04	1.03	1.00	0.67	–	0.48	0.63	0.82
k in IN 718P alloy [16]	1.00	1.11	1.02	0.94	–	1.11	0.72	0.80	0.99

solidifying melt is inversely proportional to the ratio of thermal gradient to cooling rate (G/R). Thermal gradients in a weld pool are steeper at regions close to fusion boundary than those in weld interior due to the cold base metal [17, 18]. The steep thermal gradient at the fusion boundary contributes to columnar dendritic growth in a direction opposite to the heat extraction direction. However, the flat thermal gradient combined with the rapid cooling rates in the weld center results in significant undercooling leading to the formation of equiaxed dendrites.

During the formation of dendrites, elements with the partition coefficients k value lower than unity such as Nb, Ti and Mo will be rejected to the dendrite boundary. Though element C was hard to be detected, previously published papers emphasized that carbon is a strongly dendrite boundary segregation element [19, 20]. Hence, it is reasonable to assume that during the solidification of K4750, carbon would segregate to the interdendritic liquid. The interdendritic regions will be supersaturated with Nb, Ti, Mo, W and C as the dendrites continuously grow up. Therefore, the strong combination of Nb, Ti, Mo and W to C results in the formation of carbides, which can be used to explain why carbides mainly distributed in the dendritic boundaries and enriched in these elements as shown in Fig. 6b, d. It also should be noted that segregation is a time-dependent phenomenon and is strongly affected by the weld cooling rate. GTAW process with higher heat input, smaller power density and slower weld cooling rate results in relatively large dendritic arm spacing compared to electron beam process welds, and these coarse dendritic spacing provide congenial sites for alloying elements segregation during weld solidification. From this point of view, GTAW-processed IN 718 alloy and K4750 alloys welds are more prone to segregation than EB-processed IN 718P alloy welds as shown in Table 4. Furthermore, the segregation behavior is also strongly affected by atomic size difference and interactions of other alloying elements [21]. As shown in Table 4, element with similar atomic radii to Ni, namely Cr, has k value very close to unity. This is attributed to the effect of atomic size difference on solubility, where elements with similar atomic radii generally exhibit appreciable solubility. This result is in good agreement with the previous result [9]. Furthermore, an interactive effect between different elements can be used to explain the variations of k values for different elements in K4750 alloy compared with IN 718 and IN 718P alloys. More specifically, elements Fe and Ni with similar atomic radii, but they exhibit different segregation behaviors during K4750 weld metal solidification. Tungsten is prone to segregate to dendritic boundaries in K4750 weld metal whereas to dendritic cores in IN 718P weld metal.

HAZ microstructures of as-welded joints

Figure 7 shows the microstructure of HAZ adjacent to the FZ of the as-welded joint. There are no obvious lines dividing HAZ from FZ, and the grain growth is not significant in HAZ. Normal epitaxial growth of dendrites in weld fusion zone is apparent. At the same time, competitive growth of dendrites is also found at the fusion zone. As mentioned in the macrostructure analysis, no liquation cracking was found in the joint HAZ. And in the higher magnified images, liquation cracking was also not observed. MC-type carbides with eutectic morphology were observed in the HAZ just next to the fusion line as shown in Fig. 7c. The higher magnified image of the liquated carbide marked in Fig. 7c was shown in Fig. 7d. It showed a liquated matrix was around the eutectic carbide, which demonstrated that the MC carbides undergo extensive liquation during weld heating.

It also can be found that the grain boundary liquation is mainly relying on the liquation of MC carbides located at the grain boundaries. This can be explained as follows: As mentioned above, the pre-weld heat treatment of the alloy is solutionized at 1120 °C/4 h followed by air cooling. The main

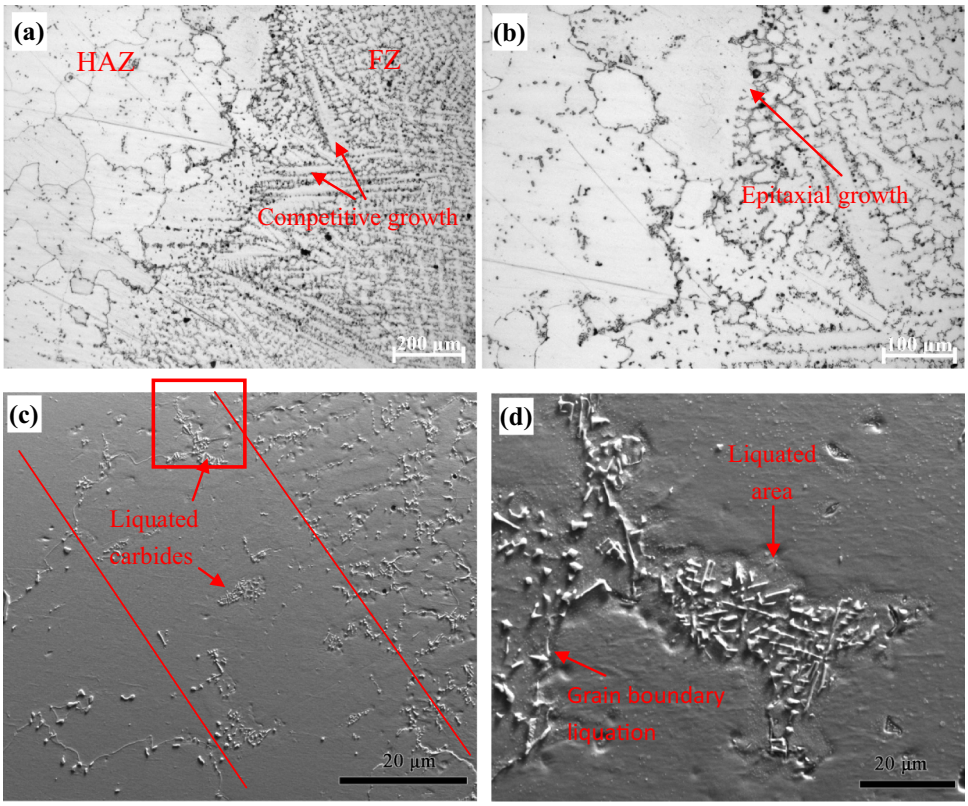

Figure 7 Microstructure of as weld joints. **a** and **b** OM image of fusion boundary, **c** SEM image of fusion boundary, **d** SEM image of liquated carbide in the joint HAZ.

strengthened precipitates γ′ and other secondary solidification products such as borides and eta phases were completely dissolved during the heat treatment. The re-precipitation of these phases during cooling stage from the solution heat treatment was suppressed due to the fast air cooling rate. Therefore, no grain boundary γ′ and/or other secondary solidification products liquation can be taken place at the joint HAZ. Furthermore, other impurity elements such as Zr and S are also in a very low level. So the low melting point phases enriched in Zr, B and S are not found. Thus, the grain boundary liquids are mainly from the liquation of MC-type carbides located at the grain boundary.

The epitaxial growth dendrites in weld fusion zone boundary indicate that the dendrites grow in a different direction depending on the orientation of the grains in the base material. At the same time, the competitive growth dendrites are also found at the fusion zone boundary due to the different growth directions of the epitaxial growth dendrites combined with the thermal gradient direction within the fusion zone. The absence of liquation cracking in the as-welded joint HAZ suggests that K4750 alloy possess excellent liquation cracking resistance. Liquation cracking occurrence is often reported in precipitation-strengthening nickel-based superalloys [22–25]. A combination of large shrinkage stresses that occur as a result of rapid precipitation of γ′ particles during cooling and very low ductility in the alloy due to localized melting at grain boundaries related to constitutional liquation of phases present on them results in HAZ liquation cracking. The precipitation rate of γ′ is mainly related to the volume fraction of γ′, which is controlled by the concentration of γ′ forming elements such as Al and Ti. Alloys with high concentration of these elements will promote γ′ particles precipitation with large number and fast speed, which results in high shrinkage stresses. The total amount of Al + Ti in K4750 alloy is approximate 4.4 wt% which is relatively low compared to other casting superalloys [22–26]. The lower content of γ′ precipitates results in small shrinkage stress during weld solidification which improves the liquation cracking resistance. In addition, the low microstructural sensitivity due to pre-weld solution heat treatment also attributes to the high cracking resistance property. It is well known that the region closer to the welding fusion line always experiences higher temperature during welding. When the temperature exceeds the

precipitates dissolved temperature, liquation of the undissolved precipitates will take place. Ashby and Easterling [27] derived a particle dissolution model and they verified the model experimentally. They showed that there is a significant departure from equilibrium under rapid heating condition. The temperature of complete solid-state dissolution increased with increasing heating rate, and the extent of this departure is dependent on the initial particle size and the heating rate. The pre-weld material was subjected to solution at 1120 °C for 4 h which completely dissolved the γ′. Though some γ′ particles will re-precipitate during cooling from pre-weld heat treatment, the size of the re-precipitate particle is too small and hard to be revealed by SEM due to the fast cooling rate. Therefore, the constitutional liquation tendency of γ′ particles can be decreased. The occurrence of liquated MC carbides within joint HAZ but without liquation cracking reveals that the thermal stress induced by welding could not lead to cracking.

Microstructures of the PWHT joints

Figure 8 shows typical microstructure of the PWHT joints. The HAZ cracks were also not observed at the joints, indicating K4750 alloy owned excellent resistance to strain-age cracking. It is also presented that the recrystallized grains can be observed in the fusion zone. Note that before PWHT, all the grains in the FZ exhibited dendritic morphology as shown in Fig. 6. The eutectic MC-type carbides without the surrounding liquated matrix in HAZ show the post-weld solution heat treatment temperature is able to eliminate the liquated matrix. It is noted in SEM images shown in Fig. 8d that except for the MC-type carbides, discretely distributed grain boundary precipitates can also be detected both in the HAZ and fusion zone. A more detail study on the grain boundary precipitates was carried out by TEM examination as shown in Fig. 9. It has been confirmed that the grain boundary precipitates are Cr-rich $M_{23}C_6$-type carbide with a complex cubic crystal structure with the lattice parameter of approximate 10.64 Å. In addition, the presence of spherical γ′ particles with the diameter about 50 nm was revealed by the TEM dark-field image as well.

The occurrences of recrystallized grains suggest the presence of thermal stress during the welding operations, leading to a high density of dislocations, the driving force for recrystallization. Strain-age cracking (SAC) is often occurred during post-weld heat treatment as a consequence of welding thermal stress combining with the low ductility microstructure formed during welding. It was widely reported in many kinds of γ′ precipitation-hardened superalloys joint HAZ [24, 27–30]. Low ductility microstructure formed during welding often implies the formation of liquated precipitates and grain boundaries. The occurrence of eutectic morphology MC carbides indicating liquation of the MC carbides is mentioned in "Fusion zone solidification" section. The strain-age crack-free HAZ indicates low welding thermal stresses, due to easy stress relaxation during PWHT and therefore may be responsible for the preclusion of SAC in joint HAZ observed in the present work. Prager pointed that the susceptibility of strain-age cracking in precipitation-strengthening superalloys is most related to the content of γ′ former elements such as Al and Ti [31]. When the amount of Al + Ti is over 6 wt%, it will result in high susceptibility of SAC. The reason is that the higher amount of Al and Ti in superalloy, the more γ′ will precipitate during PWHT heating stage which results in larger precipitate contraction stress. And the high volume fraction of γ′ precipitates will result in large hardness of base material which increases the difficulty of welding residual stress relaxation. In addition, high volume fraction of γ′ precipitates results in high tendency of constitutional liquation of γ′ precipitates which contributes to low ductility microstructure thus causing high SAC sensitivity. As mentioned previously, the maximum amount of Al and Ti in K4750 alloy is 4.4 wt%, which is lower than the critical composition level. The decreased γ′ precipitates liquation tendency by pre-weld solution heat treatment further reduces the HAZ microstructure susceptibility. So K4750 alloy has excellent HAZ strain-age cracking resistance properties. Cr-rich $M_{23}C_6$ carbides which are able to partly pin the migrated grain boundaries and impede their motion away from the parent solidification grain boundary in nickel-based superalloys are reported to form as a result of the reaction of MC carbides with γ matrix MC → $M_{23}C_6$ + γ′. They can form either during PWHT of precipitation-strengthened nickel-based superalloys in a large temperature range of 600–1050 °C or during high-temperature exposure in the service.

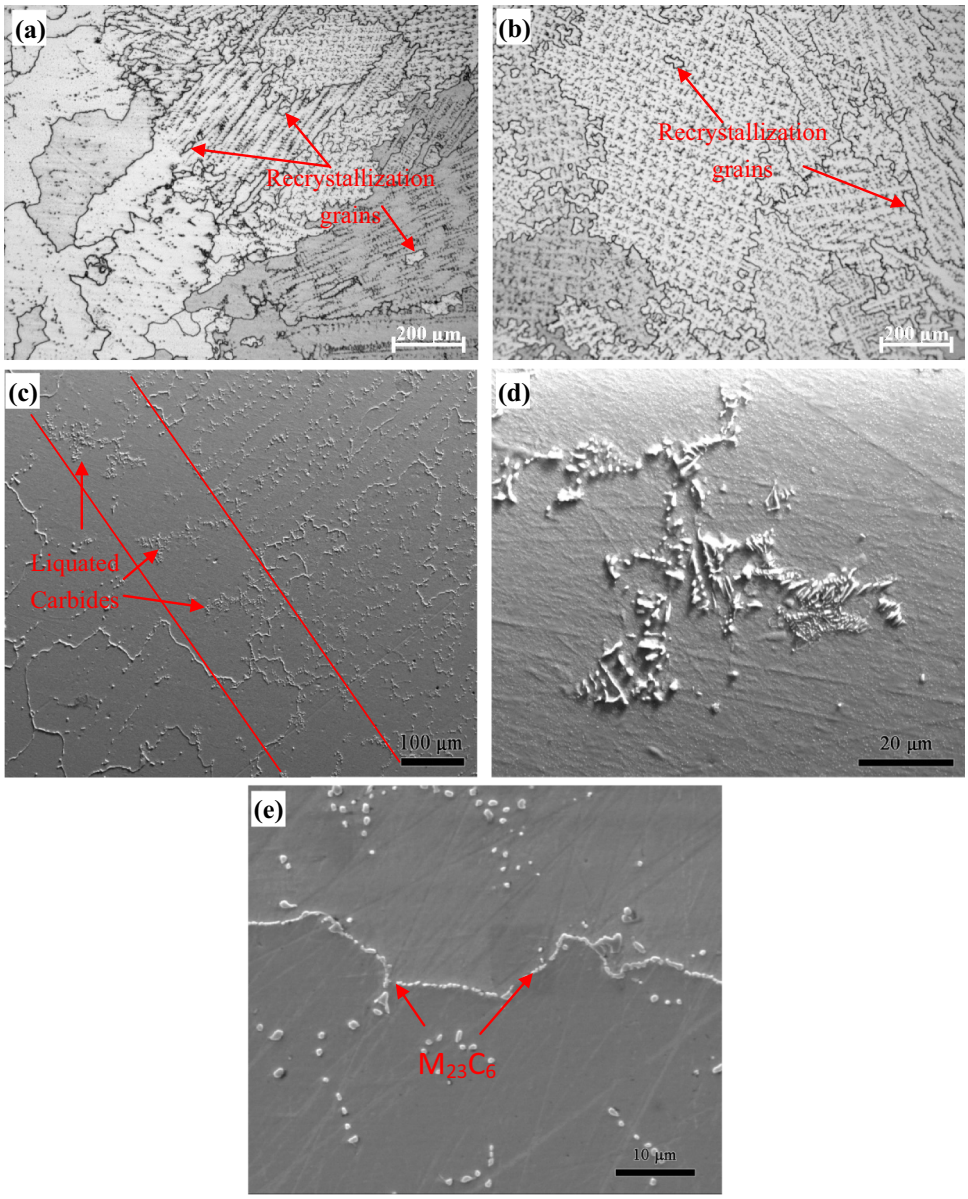

Figure 8 Microstructure of the PWHT joint. **a** OM image of fusion boundary, **b** OM image of fusion zone, **c** and **d** SEM image of HAZ, **e** SEM image of fusion zone.

Microhardness distribution

The microhardness profiles across the weld cross section with different conditions are shown in Fig. 10. Obviously, the post-weld heat-treated joints exhibited higher hardness values than those of the as-welded joints across the whole weld cross section. In the as-welded samples, the average microhardness values of the fusion zone are about 250Hv. The microhardness values of the base metal and HAZ are about 300Hv, except for some peaks with extremely high hardness values. The microhardness fluctuations in base metal are related to the randomly distributed MC carbides at the interior of the grains and/or the grain boundaries, as seen in Fig. 4b. In the PWHT sample, the microhardness values across the whole cross section are nearly fluctuated around 380Hv indicating that the microstructure was homogenized within the whole cross section.

The hardness results are important since weld strength mismatch is a major concern when welding most metallic materials. The γ′ precipitation hardening effect is responsible for the hardness increment from the as-welded joint to the post-weld heat-treated joint. It is also related to the lower hardness value at the fusion zone compared to the base metal in the as-welded sample. Because the γ′ precipitation in the as-welded fusion zone were suppressed by rapid

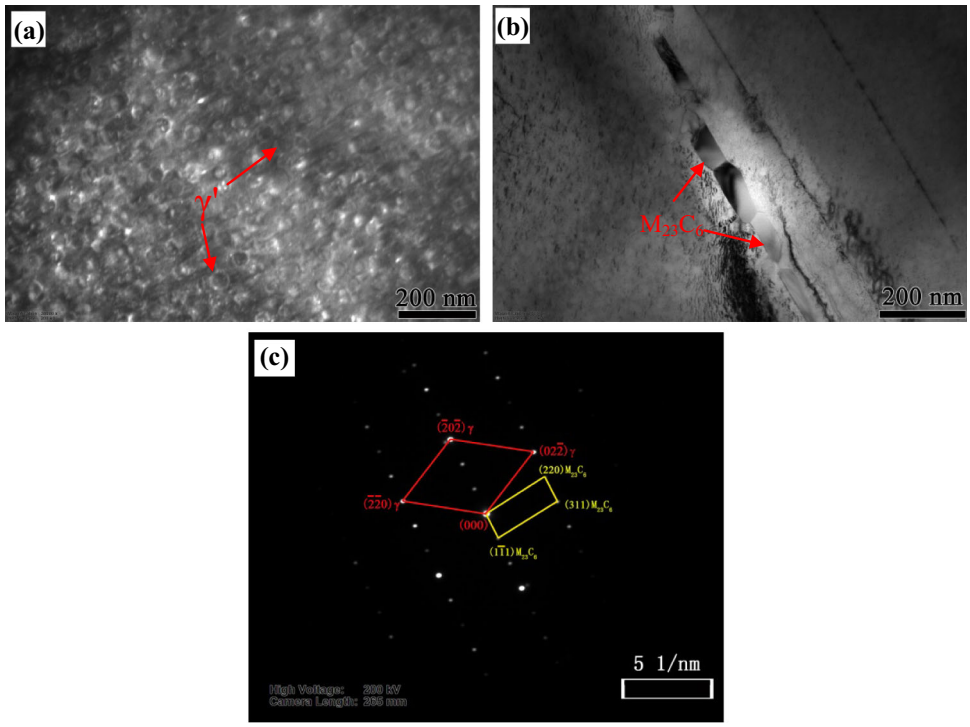

Figure 9 TEM images of the PWHT joint fusion zone. **a** Dark-field image of γ′ particles in fusion zone **b** fusion zone grain boundary precipitates **c** SADP image of grain boundary precipitates.

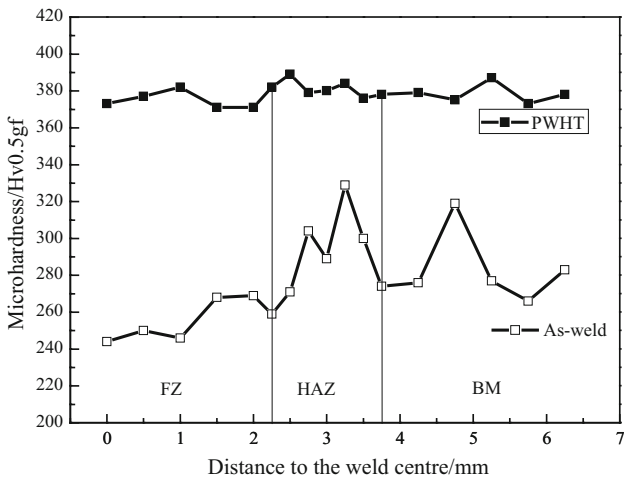

Figure 10 Microhardness profiles of the joints in different conditions.

cooling rate from welding solidification as shown in Fig. 6. After PWHT, the γ′ precipitates formed within the fusion zone as shown in Fig. 9 significantly increase the fusion zone microhardness. The amount and the size of γ′ precipitates formed within the fusion zone same as that in the base metal due to the filler material selected in the present study have same chemical compositions as the base metal. Thus, the microhardness of the post-weld heat-treated joints was in a steady level of 380Hv. As a precipitation hardening superalloy, different size and distribution of the γ′ precipitates largely affect the hardness values. Also, the uneven microstructure of the as-welded joint HAZ affects the hardness distribution significantly.

Tensile properties

The weld tensile properties in as-welded condition and the post-weld heat-treated condition are shown in Table 5. The ultimate tensile strength (UTS), yield strength (YS) and elongation of the as-welded joints are 799 MPa, 491 MPa and 27%, respectively. While as for the post-weld heat-treated joints, these values are 814 MPa, 699 MPa and 5%, respectively. The as-welded joints failed in the HAZ of the joint, while the post-weld heat-treated joints failed at the base metal far away from the weld metal as can be seen from the fracture location shown in Fig. 11. SEM images of fracture surfaces of tensile-tested samples are shown in Fig. 12. The as-welded joint fracture surface shows tearing edge and dimple-like morphology indicating ductile mode of failure. Brittle fracture feature clearly shows intergranular morphology where the fracture propagated along the dendrites can be observed in the post-weld heat-treated joints fracture surface. Furthermore, MC carbides were also found at the fracture surface.

Table 5 Room-temperature tensile properties of the joints

Condition	UTS/MPa	YS/MPa	Elongation/%
As welded	799	491	27
PWHT	814	699	5

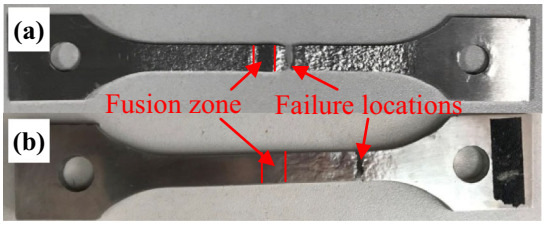

Figure 11 Fracture locations of joints with different conditions. **a** As-welded joints, **b** PWHT joints.

The post-weld heat treatment resulted in a tiny increase in the UTS and a significant increase in the YS, while the post-weld heat-treated joints also exhibited inferior elongation compared to the as-welded joints. Damodaram et al. [32] also observed that PWHT results in a significant increase in the yield strength and ultimate tensile strength compared with the as-welded condition in friction-welded IN 718 alloy. The increase in tensile strength and the decrease in elongation of the post-weld heat-treated joints are mostly related to the formation of γ' strengthening precipitates and $M_{23}C_6$ grain boundary carbides. The γ' precipitates and discretely distributed grain boundary carbides formed during PWHT strengthened the joint which leads to a lower elongation due to the difficulty of dislocation movement and hard deformation during tensile test. The cracks nucleated at the interface of the carbides and matrix also suggest the inferior effects of the large blocky MC-type carbides to the tensile elongation. The fine carbides in the weld fusion zone of the as-welded joint act as dispersions strengthened particles. However, the liquated matrix adjacent to the carbides and the completely dissolved γ' within the HAZ are detrimental to the tensile strength, which was proved by the fracture location of the as-welded joints (Fig. 11). In addition, large eutectic carbides may act as crack initiators to be detrimental to the properties of the joints to some extent [33, 34]. The disappearance of liquated matrix around the eutectic morphology MC carbides in PWHT joint HAZ may recover the strength of the area, which results in the

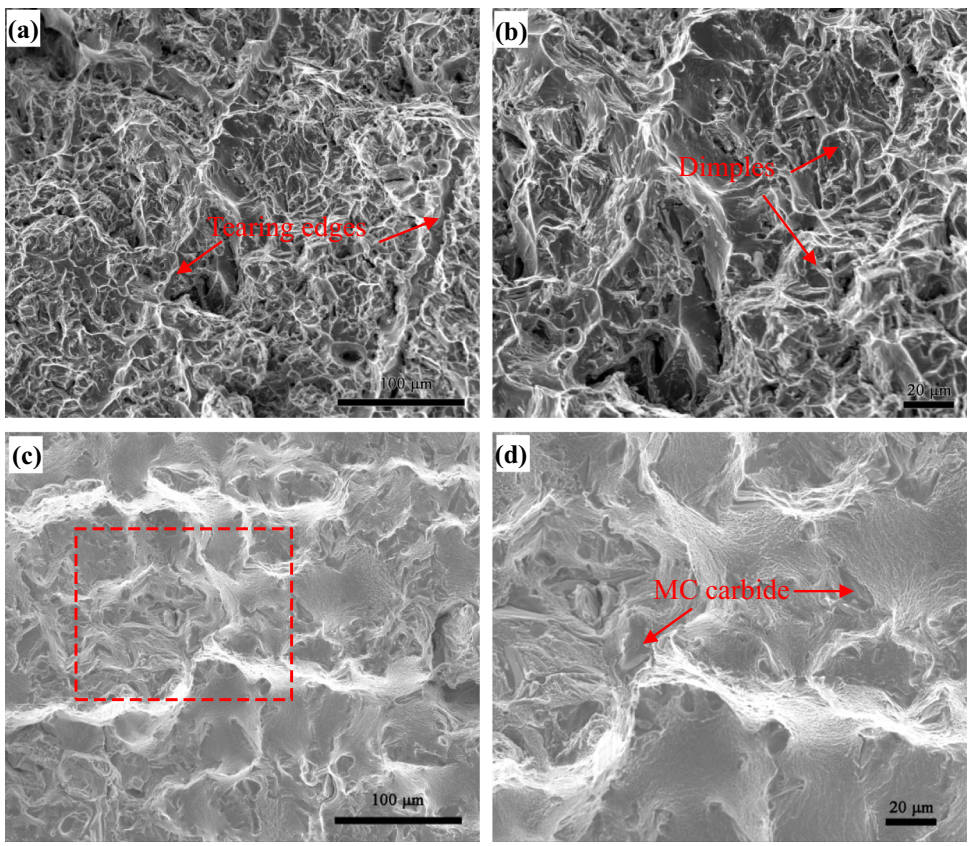

Figure 12 Tensile fracture surfaces morphologies of joints with different conditions. **a** and **b** As-welded joints, **c** and **d** PWHT joints.

failure location away from it. The tensile properties of the as-welded and the post-weld heat-treated joints of K4750 alloy are comparable to the GTAW-processed IN 718 joints [35]. In addition to the room-temperature properties, as a new superalloy aimed to use at temperature around 750 °C, high-temperature properties of the welded joints also need to be taken into consideration and the high-temperature tensile test of the welded joints will be conducted in the future.

Conclusions

The newly designed nickel-based superalloy named K4750 was subjected to manual GTAW processing. The microstructures and mechanical properties of the joints in various conditions were studied. The following conclusions can be drawn.

1. K4750 alloy has excellent HAZ cracking resistance due to the relative low content of Al and Ti elements.
2. The microsegregation observed during solidification of the K4750 alloy weld fusion zone indicated that Fe was prone to segregate into the dendritic core, while Nb, Mo, Ti, W and Si were rejected into the dendritic boundary.
3. The phase transformation sequence of K4750 alloy fusion zone is as follows: $L \rightarrow L + \gamma \rightarrow L + \gamma + (Ti, Nb)C \rightarrow \gamma + (Ti, Nb)C$.
4. The tensile properties of the as-welded joints are comparable to the PWHT joints in terms of the UTS and the elongation.

Acknowledgements

The authors would like to sincerely thank Mr. Lei Shu and Mr. Zhanhui Du for providing the welding materials.

Compliance with ethical standards

Conflict of interest The authors declare that they have no conflict of interest.

References

[1] Reed RC (2006) The superalloys fundamentals and applications. Cambridge University Press, New York

[2] Sun F, Tong JY, Feng Q, Zhang JX (2015) Microstructural evolution and deformation features in gas turbine blades operated in-service. J Alloys Compd 618:728–733

[3] Kim DH, Kim JH, Sa JW, Lee YS, Park CK, Moon SI (2008) Stress rupture characteristics of Inconel 718 alloy for ramjet combustor. Mater Sci Eng A 483–484:262–265

[4] Wang Y, Shao WZ, Zhen L, Yang C, Zhang XM (2009) Tensile deformation behavior of superalloy 718 at elevated temperatures. J Alloys Compd 471:331–335

[5] Lingenfelter A (1989) Welding of Inconel 718—a historical review. In: Conference proceedings on superalloy 718—metallurgy and applications, TMS-AIME, Warrendale, 673–683

[6] Kennedy RL (2005) 'Allvac 718Plus, superalloy for the next forty years. In: Proceedings of 6th international symposium on superalloys and various derivatives 718, 625, 706, 1–14

[7] Guédou JY, Fedorova T, Rösler J, Klöwer J, Gehrmann B, Choné J (2014) Development of a new 718-type Ni–Co superalloy family for high temperature applications at 750 °C. In: MATEC web of conferences 14, vol: 01003: 1–6

[8] Ou M, Ma Y, Ge H, Xing W, Zhou Y, Zheng S, Liu K (2018) Microstructure evolution and mechanical properties of a new cast Ni-base superalloy with various Ti contents. J Alloys Compd 735:193–201

[9] John JCL, DuPont N, Kiser Samuel D (2009) Welding metallurgy and weldability of nickel-base alloys. John Wiley & Sons Inc, Hoboken

[10] Idowu∗ OA, Ojo OA, Chaturvedi MC (2007) Effect of heat input on heat affected zone cracking in laser welded ATI Allvac 718Plus superalloy. Mater Sci Eng A 454–455:389–397

[11] Arulmurugan B, Manikandan M (2017) Development of welding technology for improving the metallurgical and mechanical properties of 21st century nickel based superalloy 686. Mater Sci Eng A 691:126–140

[12] Shi Z, Dong J, Zhang M, Zheng L (2013) Solidification characteristics and segregation behavior of Ni-based superalloy K418 for auto turbocharger turbine. J Alloy Compd 571:168–177

[13] Yin H, Gao Y, Gu Y (2017) Evolution of the microstructure and microhardness of the welding joint of IN 740H alloy with IN 617 as filler metal. Mater Charact 127:288–295

[14] Seo S-M, Jeong H-W, Ahn Y-K, Yun DW, Lee J-H, Yoo Y-S (2014) A comparative study of quantitative microsegregation analyses performed during the solidification of the Ni-base superalloy CMSX-10. Mater Charact 89:43–55

[15] Paulonis DF, Oblak JM, Duvall DS (1969) Precipitation in nickel-base alloy 718. Trans ASM 62:611–622
[16] Vishwakarma KR, Richards NL, Chaturvedi MC (2008) Microstructural analysis of fusion and heat affected zones in electron beam welded ALLVAC® 718PLUS™ superalloy. Mater Sci Eng A 480:517–528
[17] David SA, Vitek JM (1992) Principles of weld metal solidification and microstructures. In: Conference proceedings on trends in welding research, 147–152
[18] Janaki Ram GD, Venugopal Reddy A, Prasad Rao K, Reddy GM, Sarin Sundar JK (2005) Microstructure and tensile properties of Inconel 718 pulsed Nd-YAG laser welds. J Mater Process Technol 167(1):73–82
[19] Knornovsky GA, Cieslak MJ, Headley TJ, Romig AD Jr, Hammetter WF (1989) Inconel 718: a solidification diagram. Metall Trans A 20A:58–2149
[20] Thompson RG, Mayo DE, Radhakrishann B (1991) A phase diagram approach to study liquation cracking in alloy 718. Metall Trans A 22A:67–557
[21] Radhakrishna C, Prasad Rao K (1997) The formation and control of Laves phase in superalloy 718 welds. J Mater Sci 32:1977–1984. https://doi.org/10.1023/A:1018541915113
[22] Richards NL, Nakkalil R, Chaturvedi MC (1994) The influence of electron-beam welding parameters on heat-affected-zone microfissuring in INCOLOY 903. Metall Mater Trans A 25(8):1733–1745
[23] Ojo OA, Richards NL, Chaturvedi MC (2004) Liquation of various phases in HAZ during welding of cast Inconel* 738LC. Mater Sci Technol 20(8):1027–1034
[24] Rush MT, Colegrove PA, Zhang Z, Broad D (2012) Liquation and post-weld heat treatment cracking in Rene 80 laser repair welds. J Mater Process Technol 212(1):188–197
[25] Chauvet E, Kontis P, Jägle EA et al (2018) Hot cracking mechanism affecting a non-weldable Ni-based superalloy produced by selective electron beam melting. Acta Mater 142:82–94
[26] Jahangiri MR, Arabi H, Boutorabi SMA (2013) Development of wrought precipitation strengthened IN939 superalloy. Mater Sci Technol 28(12):1470–1478
[27] Ashby MF, Easterling KE (1982) A first report on diagrams for grain growth in welds. Acta Metall 30:78–1969
[28] Sidhu RK, Richards NL, Chaturvedi MC (2007) Post-weld heat treatment cracking in autogenous GTA welded cast Inconel 738LC superalloy. Mater Sci Technol 23(2):203–213
[29] Lim LC, Yi JZ, Liu N (2002) Mechanism of post-weld heat treatment cracking in Rene 80 nickel based superalloy. Mater Sci Technol 18(4):407–412
[30] Dix AW, Savage WF (1971) Factors influencing strain-age cracking in Inconel X-750. Weld J 50:247s–252s
[31] Prager M, Shira CS (1968) Welding of precipitation-hardening nickel-base alloys. WRC Bull 128:1–55
[32] Damodaram R, Raman SGS, Rao KP (2014) Effect of post-weld heat treatments on microstructure and mechanical properties of friction welded alloy 718 joints. Mater Des 53:954–961
[33] Lu L, Soda H, McLean A (2003) Microstructure and mechanical properties of Fe–Cr–C eutectic composites. Mater Sci Eng A 347:214–222
[34] Briggs R (1965) Molten-salt reactor program semiannual progress report. ORNL 3812:71–72
[35] Wang Q, Sun DL, Na Y, Zhou Y, Han XL, Wang J (2011) Effects of TIG welding parameters on morphology and mechanical properties of welded joint of Ni-base superalloy. Proced Eng 10:37–41